ADVANCED MATERIALS TECHNOLOGIES
www.advmattechnol.de

3D-Printed Bioreactor with Integrated Impedance Spectroscopy for Cell Barrier Monitoring

*Georg Linz, Sebastian Bernhard Rauer, Yasmin Kuhn, Simon Wennemaring, Laura Siedler, Smriti Singh, and Matthias Wessling**

Cell culture experiments often suffer from limited commercial availability of laboratory-scale bioreactors, which allow experiments to be conducted under flow conditions and additional online monitoring techniques. A novel 3D-printed bioreactor with a homogeneously distributed flow field enabling epithelial cell culture experiments and online barrier monitoring by integrated electrodes through electrical impedance spectroscopy (EIS) is presented. Transparent and conductive indium tin oxide glass as current-injecting electrodes allows direct visualization of the cells, while measuring EIS simultaneously. The bioreactor's design considers the importance of a homogeneous electric field by placing the voltage pick-up electrodes in the electrical field. The device's functionality is demonstrated by the cultivation of the epithelial cell line Caco-2 under continuous flow and monitoring of the cell layer by online EIS. The collected EIS data were fitted by an equivalent electric circuit, resulting in the cell layer's resistance and capacitance. This data is used to monitor the cell layer's reaction to ethylene glycol-bis-(2-aminoethyl ether)-*N,N,N′,N′*-tetraacetic acid and forskolin. These two model substances show the power of impedance spectroscopy as a non-invasive way to characterize cell barriers. In addition, the bioreactor design is available as a print-ready file in the Appendix, enabling its use for other scientific institutions.

1. Introduction

Barrier-forming epithelial and endothelial tissues possess a unique ability to form cell-to-cell connecting tight junctions that create compartmentalization in multicellular organisms and prevent unhindered diffusion across cellular barriers.[1] The ability to regulate the transport of molecules is essential in supplying tissues with nutrients, removing toxic compounds, or preventing the invasion of pathogens into deeper tissues. However, this barrier function of epithelial and endothelial tissues can pose a significant obstacle like in the case of blood–brain barrier where the cellular barrier also hinders therapeutic substances from entering and thereby reaching target tissues in the body.[2] The recent pandemic of SARS-CoV-2 accesses the host cells through the receptors on the lung alveolar barrier.[3] Therefore, understanding the pathophysiology of various cellular barriers is crucial for fundamental and pharmaceutical research.[4]

The standard technique for in vitro cell barrier experiments is the static cultivation of epithelial or endothelial cells on semipermeable membranes in transwell inserts, which allow access to the apical and basal sides of the cell layer. However, standard in vitro cultivation cannot mimic the complex physiological conditions present within the human body, such as the exposure of cells to shear stress in their natural environment. To mimic the respective in vivo environment in in vitro models, "organ-on-a-chip" research targets the engineering of bioreactor systems to provide a higher degree of physiology.[5]

The main prerequisite for conducting experiments on biological barriers is to ensure barrier integrity. The most prominent barrier integrity tests are either based on the retention of macromolecules, non-invasive electrical resistance, or impedance measurements.[6] Electrical impedance is the extension of Ohm's law from direct current to alternating current. The impedance Z is defined as the quotient of the time-dependent voltage U_t and current I_t. The general approach for electrical impedance spectroscopy (EIS) is to apply a small voltage or current with varying frequencies to electrodes and measure the resulting current or voltage. By fitting the EIS spectra to an equivalent electric circuit, different transport phenomena across a barrier can be extracted.[7]

In this study, we aimed to present a 3D printed micro bioreactor for the cultivation of epithelial cells with EIS. The integrated four-electrode EIS allows online monitoring of the cell barrier resistance and capacitance. We demonstrated the reactor's functionality by cultivating Caco-2 epithelial cells under continuous flow conditions, as well as monitoring the reaction to ethylene glycol-bis-(2-aminoethyl ether)-*N,N,N′,N′*-tetraacetic acid (EGTA) and forskolin by EIS.

G. Linz, Dr. S. Singh, Prof. M. Wessling
DWI-Leibniz-Institut für Interaktive Materialien
Forckenbeckstraße 50, 52074 Aachen, Germany
S. B. Rauer, Y. Kuhn, S. Wennemaring, L. Siedler, Prof. M. Wessling
RWTH Aachen University, Chemical Process Engineering
Forckenbeckstraße 51, 52074 Aachen, Germany
E-mail: Manuscripts.cvt@avt.rwth-aachen.de
The ORCID identification number(s) for the author(s) of this article can be found under https://doi.org/10.1002/admt.202100009.

DOI: 10.1002/admt.202100009

2. Background

Fluid shear stress can be applied to cells by continuous perfusion of a medium in a cell culture bioreactor.[8–11]

For example, epithelial cells lining the walls of the gastrointestinal tract are continuously exposed to shear stress resulting from in vivo peristaltic movement. These mechanical forces on the cell barrier are of major importance for their differentiation and function.[12] To accurately mimic the natural cellular environment and therefore provide a physiological culture environment, incorporating the latter physical factor into the bioreactor system is necessary. A defined medium flow during cultivation yields specific shear stress on the cells. Typical shear stress in the human intestine was reported to range from 0.002 to 0.08 dyne cm^{-2}.[13] Furthermore, the application of fluid shear stress on cells was found to stimulate cell proliferation and accelerate the differentiation process.[8,12,14]

2.1. Additive Manufacturing for Bioreactor Designs

Most tissue reactor designs on micro-scale rely on polydimethylsiloxane (PDMS)-based replica molding.[15] Even though this fabrication technique is a valuable tool in disease modeling and other organ-on-chip applications, device design and fabrication require special facilities.[16] Direct additive manufacturing of tissue reactors offers an alternative to replica molding to overcome the limitation of layered structures and extend the devices to a 3D complexity.[17] We showed a combination of PDMS-based replica molding and 3D printing as a valuable tool for high precision nanofabrication[18] and the complete replacement of a molding method for reactor fabrication.[19] The latter example uses a polyjet printer that can print a polyethylene-like polymer with high resolution and high fabrication speed. This printer has already been in use for producing customized tissue reactors.[20,21] Regardless of the tissue reactor fabrication method, the integration of microsensors enables non-invasive online analytics and is valuable in the operation of a microreactor. Metabolite concentration, dissolved oxygen, and pH,[22] and with a focus on barrier-forming tissue, resistance measurement,[23] are of great interest.

2.2. Electrode Integration for EIS

Placing electrodes inside the microenvironment of a bioreactor is challenging due to the limited space. Various approaches have been presented in the literature. Some methods include the patterning of the upper and lower surfaces of the cultivation chamber with electrodes by sputtering,[24] printing,[14] or inserting metal wires into the device.[25] We used a hybrid method in which the complete upper and lower areas of the cultivation chamber are a current-carrying electrode producing an almost homogeneous electrical field along the *x*-*y*-plane. Additionally, two platinum wires were placed in the homogeneous electrical field and proximity to the cell barrier, functioning as voltage pick-up electrodes. This electrode configuration allows EIS without unwanted phase-shifts between voltage and current and enables electric circuit fitting.

Often, integrated electrodes are only used to calculate resistance and not impedance.[26–28] In principle, integrated electrodes for resistance measurement can be used for EIS. The input signal needs to be changed from direct current or single frequency, as used in voltohmmeter (EVOM or Millicell), to a frequency spectrum.[29] In cell-barrier research, often frequencies from 10 Hz to 100 kHz are used. Impedance spectroscopy has two significant advantages compared to resistance measurements. First, the contribution of the cell layer resistance can be distinguished from medium resistance without measuring a blank probe without cells. Second, the cell layer capacitance can be extracted from the impedance spectrum, which can also be used to monitor cell layers.[30,31]

2.3. Importance of Four Electrode Impedance Spectroscopy

Electric current applied to electrodes inside a conductive solution evokes counter-charged ions to move toward the electrode and form an ionic double layer. The electrode/electrolyte interface stores charges and hence behaves as a capacitor. The formation of an electric double-layer on the surface of a current-carrying electrode and the measurement of associated frequency-dependent impedance is a major challenge in EIS on biological materials because the impedance of such an electrode/electrolyte layer is similar to that of a biological barrier. The electric double-layer impedance depends on the electrolyte's conductivity and temperature, electrode structure, composition, and roughness, and adds a great uncertainty to the system, which can lead to possible misinterpretation of the impedance spectrum.[32] This electrode surface effect should be considered in EIS. Efforts have been made to minimize the double-layer formation by platinization of electrodes,[33] considering the formation in the equivalent electrical circuit,[25] or by using four electrodes to separate the current-carrying electrodes from the measuring electrode.[34]

In the case of a four-electrode setup, additional considerations are necessary with regard to the placement of the electrodes within the micro-bioreactor. In this context, geometrical effects, especially, may alter the impedance spectra significantly. Therefore, the potential pick-up electrodes must be placed to prevent the shifting of the equipotential lines between high and low-frequency.[35] Other sources of errors in four-electrode EIS are presented by Grimnes and Martinsen.[36] They described unwanted phase-shifts between current and voltage when separate current paths exist, making standard electric circuit fitting impossible. Additionally, not all areas contribute equally to the impedance. Areas closer to the electrodes contribute more to overall resistance than areas located further away.[37]

A possibility for minimizing the contribution of geometrical and electrode surface effects on the impedance is the application of a modified Ussing chamber.[38] Two current-carrying electrodes are adjusted planar to the cell layer, and the voltage pick-up electrodes are placed axially to the homogeneous field.

2.4. Electric Circuit Modeling

Our approach for the development of the used equivalent electric circuit for a cell layer is explained in detail elsewhere.[29] In short, layers of epithelial or endothelial cells are often modeled as a resistor and capacitor in parallel. The resistor represents the ability to allow ions to pass through the paracellular and

transcellular pathways, and is therefore widely used as a parameter for the cell layer's integrity.[4,31] The capacitor represents the impermeability of the phospholipid membrane toward ions and the corresponding formation of an ionic double-layer on the membrane surfaces. Therefore, the capacitance can be used to detect alterations associated with the cell membrane, and further analyze folding,[39] variation in membrane composition,[40] and cell-substrate interaction.[29]

3. Results and Discussion

3.1. Simulation

The fluid flow simulation reveals laminar and homogeneous flow distribution from 0.05 to 5.00 mL min^{-1}. Representative of all simulated flow velocities is the streamlines shown in **Figure 1** in the left upper corner. The simulated streamlines visualize the box plot results and demonstrate the presence of an equally distributed flow regime in the chamber located above the cultivation membrane. The box plot in Figure 1 shows only a slight increase in the shear rate distribution by an increase in the flow rate of up to 5.00 mL min^{-1}. A further increase in the flow rate causes vortices in the cultivation chamber, which leads to a broader distribution of shear rates in the cultivation area.

However, the fluid simulation shows that the shear rate can be tailored according to the specific cell or experimental needs by varying the pump rate. In the presented bioreactor, a shear rate up to 0.2 dyne cm^{-2} can be applied. Higher shear rates might be of interest for the cultivation of endothelial cells but cannot be achieved with the current reactor design. Reducing the cultivation chamber height presents one possible solution for increasing the shear rate. However, smaller chamber dimensions also complicate the integration of the voltage pick-up electrodes necessary for EIS measurements. Another possibility for a higher shear rate would be bigger inlet and outlet channels, which would allow higher flow rates without the formation of vortices.

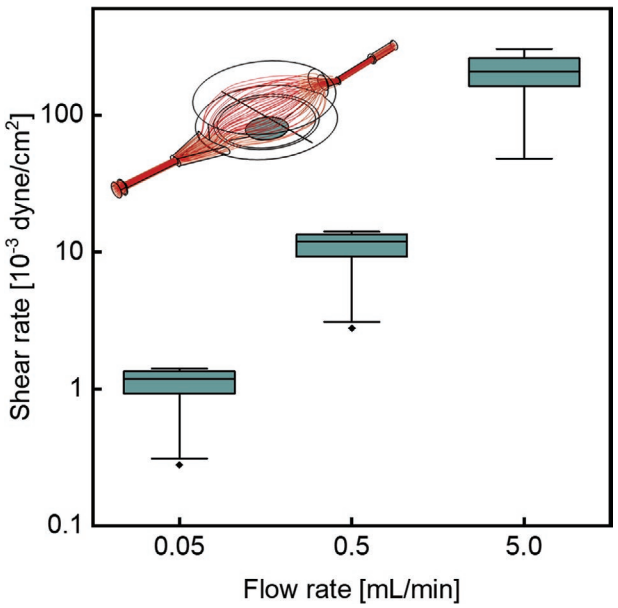

Figure 1. The box plot representation shows the mean value and the distribution of the simulated shear stress at three different flow rates on the membrane surface grouped by quartiles (boxes and bars). On the left upper corner, the streamlines indicate a homogeneous fluid distribution inside the bioreactor without vortices above the cultivation area.

Electrical field simulations allow for the visualization of the homogeneity of the electric field, while sensitivity studies reflect the contribution of a given volume or area to the total impedance. In **Figure 2**, the electric field between the current-carrying electrodes is highlighted. The membrane with the cell-layer is located in the middle of the device orthogonal to the electric field lines. The sensitivity distribution at the cell culture location is presented in Figure 2B. The sensitivity plot shows for most of the cultivation area, a homogeneous distribution. Only the edges possess a higher sensitivity due to the device geometry. On the one hand, a broader cultivation area would lead to a lower sensitivity distribution. On the other hand, the fluid shear stress distribution would be broadened. In the bioreactor presented, a compromise was made between the sensitivity and flow field distributions.

3.2. Electrochemical Impedance Spectroscopy

According to the theory of separating the current-carrying electrodes from voltage-sensing electrodes, no double-layer formation can be observed. Therefore, only ohmic resistance from the media, electrodes, and membrane can be measured without a significant phase shift between voltage and current, when no cells are in the bioreactor. The Nyquist plot representation of an EIS measurement without a cell layer can be seen in **Figure 3**, which indicates the frequency-independent impedance of a pure resistor.

A complete cell layer equivalent electric circuit would separate the paracellular- and transcellular pathways by taking both into account as a resistor. However, since paracellular and transcellular pathways are resistors in parallel and therefore not distinguishable by EIS, an additional method, for example, tracer substances, should be used.[41] If not, both resistances can be modeled as one. Additionally, to paracellular and transcellular pathways, the apical and basal cell membranes should be considered in the equivalent electric circuit as capacitors parallel to a resistor. If the charged species' transport characteristics are similar between the apical and basal sides, the contributions are also not distinguishable and can be summarized. Therefore, the simplest equivalent electric circuit for a cell layer is one resistor and one capacitor in parallel. Still, during cell layer development or the variation of experimental conditions, the contributions may vary, and apical and basal sides should be considered separately. If the apical side differs significantly from the basal side, two semicircles appear in the Nyquist plot. This is, for example, the case when the cell layer was in contact with forskolin, as indicated in Figure 3.

The EIS results were not presented normalized to the cultivation area (Ωcm^2 or Fcm^{-2}). Previous studies showed that the pure normalization of the surface is erroneous;[37] in the case of fixed electrodes, data derived from the same chip is readily comparable.[24]

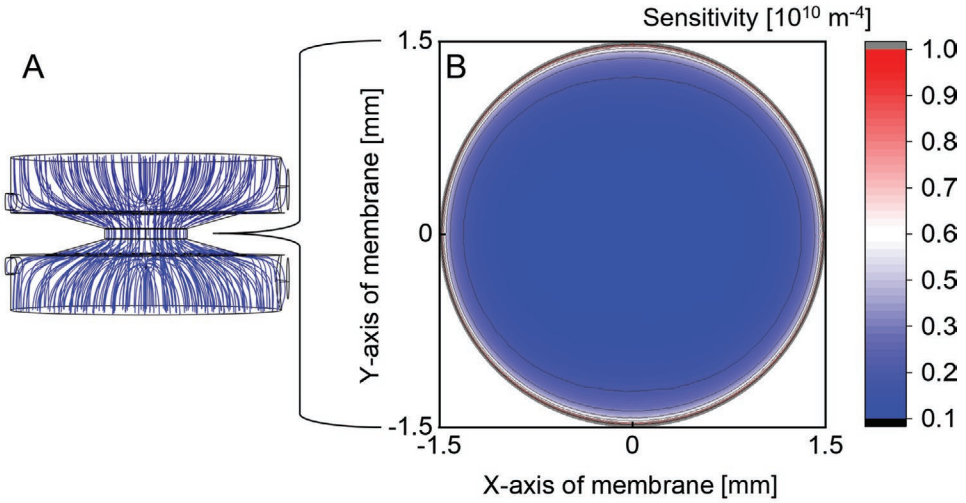

Figure 2. A) The COMSOL simulation of the electric field between the current-injecting electrodes revealed a homogeneous distribution. B) The sensitivity analysis showed for most of the cultivation area a homogeneous sensitivity distribution.

3.3. Cultivation Experiments

The confocal images in **Figure 4** of static cultivated cells in transwell inserts and dynamic cultivated Caco-2 cells reveal the importance of mimicking the fluid shear stress cells are exposed to in vivo.

The morphology of static cultivated cells showed a uniform distribution of the actin filament, as well as a layer thickness of around 20 μm. In contrast, dynamically cultured cells, which were continuously exposed to shear stress, demonstrate dislocation of the actin filament to the membrane side, as well as an increase in the cell layer thickness.

The introduced bioreactor allows visualization of the cells during cultivation. Therefore, sources of interference, such as air bubbles, can be recognized, and cellular proliferation and macroscopic changes regarding the cell layer can be readily observed. A picture of the cell layer at the beginning of a cultivation and a fully developed barrier can be seen in **Figure 5**C. In addition to visual observation, EIS allows the monitoring of the cells online. The resistance and cell layer capacitance of 14 days cultivation can be found in Supporting Information.

The addition of EGTA or forskolin demonstrated the versatility of EIS. EGTA complexes calcium ions, which are then no longer available for the formation of tight junctions. The tight junction protein complex is mainly responsible for the paracellular electrical resistance. **Figure 6** shows the course of resistance and capacitance after contact with EGTA, and the recovery when the calcium-containing medium again surrounds the cells. EGTA reduces the resistance by more than half, while the capacitance only reduces slightly. After changing the medium back to an EGTA-free medium, the resistance and capacitance recover to their starting value. The resistance needed about 3 h for recovery, whereas the capacitance recovered almost immediately.

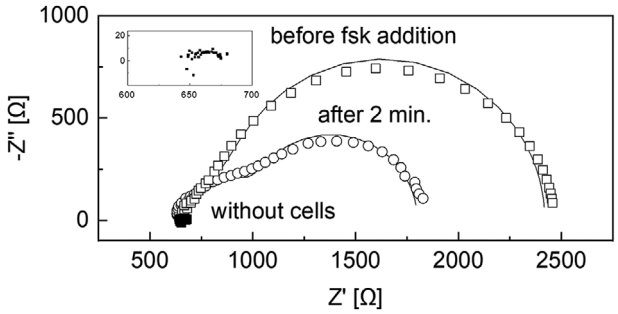

Figure 3. EIS measurement of a Caco-2 layer between 10 Hz and 30 kHz in Nyquist plot representation before and 2 min after the contact with forskolin. The cell layer was fitted with two RC-Elements in series, taking the apical and basal sides into account (Pearson's correlation Z' $r > 0.95$, Z'' $r > 0.70$). Additionally, an EIS spectrum of the medium without a cell layer is presented for comparison. The fitting values can be found in Supplementary Information.

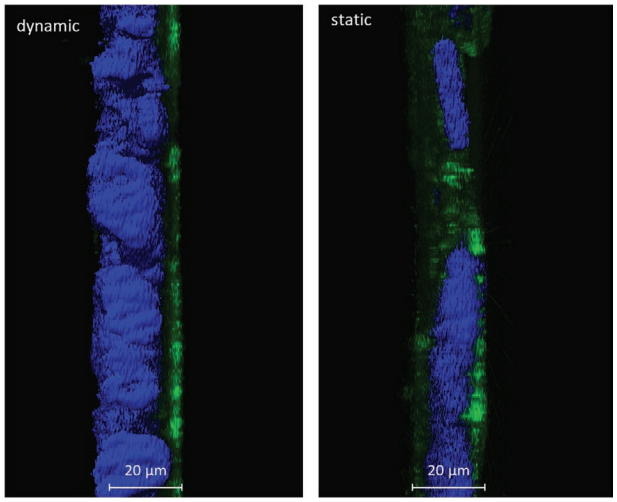

Figure 4. Lateral view of dynamic and static cultivated Caco-2 cell layers. The left side reflects the fluid side of the cells and the right side, their membrane side. The actin filament (green) was stained with Phalloidin Alexa Fluor 488 and the cell nucleus with DAPI. Pictures were taken with a Leica SP8 confocal microscope.

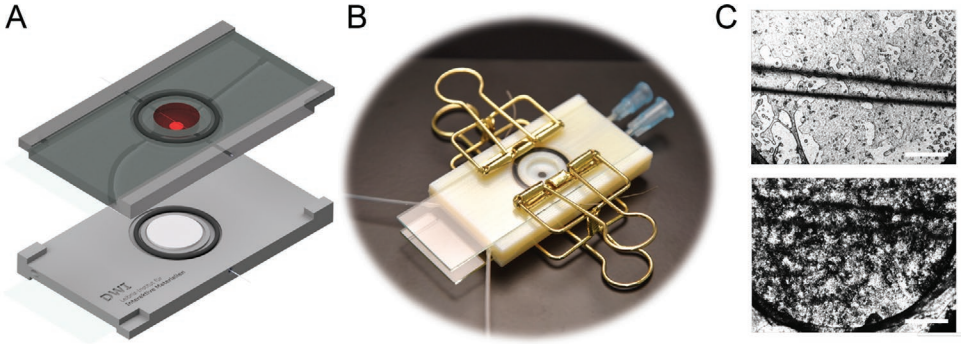

Figure 5. A) CAD model of the bioreactor displaying the two half cells with a membrane in between. The two glass slides on top and below serve as current-injecting electrodes, and the wires through the upper and lower cultivation chambers are the voltage pick-up electrodes. B) Image of the assembled bioreactor. C) Microscopy images of Caco-2 cells cultivated in the bioreactor after one day (upper image) and after 10 days (lower image). The shadows from left to right are the platinum wires serving as voltage pick-up electrodes. The scale bar represents 500 μm.

The capacitance arises from the double-layer formation of ions on the boundary layer between the ion-impermeable cell membrane and conductive electrolyte. The rapid restoration of the original capacitance illustrates the low interaction between EGTA and the cell membrane. The comparatively long recovery time for the resistance indicates an underlying biochemical process, which is in line with the theory of EGTA complexing calcium ions and therefore, disturbs the cell–cell connection.

Forskolin increases the concentration of the second messenger cyclic adenosine monophosphate (cAMP). This triggers various biological effects, for example, an upregulated anion secretion.[42–44] An increased transport of ions through the cell membrane decreases the electrical resistance. The different changes in resistance of apical and basal membranes lead to two semicircles in the Nyquist representation of the EIS spectra. This indicates a profound change in cell layer behavior. For an equivalent electric circuit model representing the cell layer in contact with forskolin, two RC-elements are necessary.

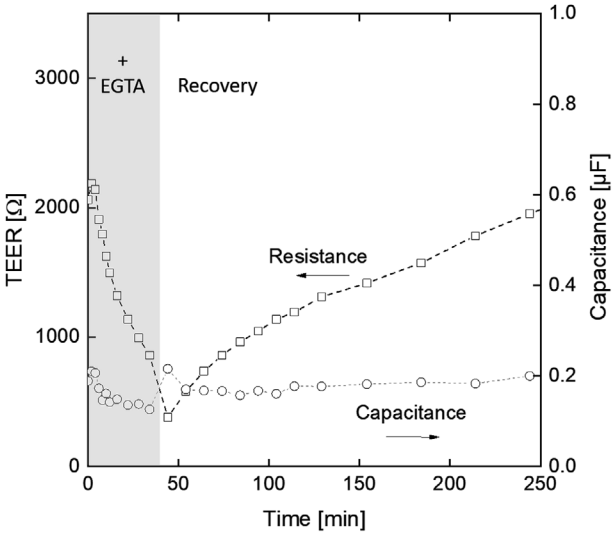

Figure 6. Resistance and capacitance over time of a Caco-2 cell layer in response to a medium containing 10 μM of the calcium chelating agent EGTA, and the recovery with EGTA-free medium. The electric properties were measured by EIS and subsequently fitted with an equivalent electrical circuit.

4. Conclusion

We demonstrated the versatility of rapid prototyping in bioreactor design or organ-on-a-chip technologies by including four electrodes for impedance spectroscopy inside the cultivation chamber for barrier-forming cells. Rapid prototyping offers advantages by a shorter development time for designing, manufacturing, and testing devices. The electric and fluid field simulation allows constructional adjustments, which can be realized directly by 3D printing. Switching the cultivation conditions from static to dynamic triggers a shear-induced cellular response, which is comparable to the cellular behavior present in the respective physiological environment. Considering that heterogeneous flow fields can lead to differently influenced cells and therefore render the interpretation of experimentally acquired data more challenging, we ensured a homogeneous flow distribution by directing the flow through a diffuser on the cell layer. The bioreactor systems allow for shear rates below 0.001 dyne cm^{-2} and up to 0.200 dyne cm^{-2} by varying the pump rate. As a result, the reactor system is particularly suited for the cultivation of epithelial cells.

In four-electrode EIS, the electrodes' positioning needs special consideration for the appropriate use of electric circuit fitting, ensuring that the measured impedance originates from the cell layer under investigation. EIS allows online and non-invasive measurement of cell layer resistance and capacitance. From resistance and capacitance, viability, integrity, and behavior of the barrier can be derived. The addition of EGTA reduces the paracellular resistance by complexing calcium ions, which are needed for tight junction protein complex. This was monitored by EIS, and in addition, the derived capacitance showed only slight changes, which indicates that the cell itself is not affected. After the EGTA treatment, the rapid restoration of the capacitance also reveals no other biological effect on the cell-layer structure. In contrast to EGTA, forskolin is known for its broad biological effects correlating with the increase in cAMP concentration. The Nyquist representation of the EIS spectra displays two semicircles and a reduction in resistance indicating a profound change in cell layer behavior.

We assume that EIS integrated into organ-on-chip or other bioreactors is a powerful tool for online analytics. Nevertheless, special attention must be paid to the positioning of the

electrodes. In this context, finding compromises among suitable positioning for EIS measurements, physiological needs of the cells, and goal of the experiment is necessary. The fabrication of our micro-bioreactor successfully demonstrates that such a compromise is achievable, and that 3D printing poses an attractive alternative to the PDMS-based production of bioreactors in research. By using additive manufacturing, geometries can be generated that are not limited to 2D replica molding. In the future, these benefits of 3D printing lab-on-a-chip devices will become even more pronounced due to further advances in 3D printing technology.

The introduced bioreactor may be beneficial for barrier-research in general by allowing the noninvasive monitoring by EIS. Influences of chemical gradients in the apical and basal chamber side on the cell barrier as well as different shear stresses can be studied.

5. Experimental Section

Bioreactor Design: The bioreactor consisted of three main parts: the 3D-printed housing, membrane, and electrodes. The 3D-printed part was designed to allow continuous medium perfusion, and therefore exposing cells to controlled, homogeneous shear stress. The bioreactor consisted of two identical half cells with a 3 mm drilling as the cultivation area. The membrane was clamped between the half cells to allow cell growth on both sides. The fluid flow on the entrance was distributed by a diffuser and directed across the membrane to apply homogeneous shear stress along the whole cultivation area. Additionally to the fluid channel, the printed chamber possessed a drilling for the platinum wire as a voltage pick-up electrode. The platinum wire was located above the membrane inside the homogeneous electrical field. The electrical field was provided by the indium tin oxide (ITO) glass functioning as current-injecting electrodes. The bioreactor was sealed by two PTFE O-rings, which are placed between the two half cells and ITO glass. To prevent a shift of the membrane position and a shortcut between the two chambers, the membrane was fixed between two PDMS rings, a biocompatible silicone polymer with self-sealing properties.

Device Fabrication and Assembly: The cell culture bioreactor was fabricated with a polyjet 3D printer (Stratasys, Objet Eden 260V). The polyjet printer can produce structures with a resolution of 42 μm (600 dpi) in x and y directions and 16 μm in the z-direction. The cultivation chamber was printed with an acrylate-based material, RGD525 (Stratasys). For producing internal channels and overhangs, the support material, SUP705 (Stratasys), was used. After the printing process, the support material was mechanically removed, and residues were dissolved in 1 mol L^{-1} sodium hydroxide solution for at least 12 h. After the cleaning step, the cultivation chamber was rinsed with water and dried. A 50 μm thick platinum wire (Goodfellow) was positioned in the wire channels and fixed with LOCTITE M-121HP HYSOL (Henkel AG) glue. The platinum wire was twisted around a 0.5 mm thick titanium wire for mechanical stability outside the bioreactor. The titanium wire is necessary for a stable connection between the bioreactor and impedance spectrometer. Polyethylene tubes (Smiths Medical) and cannulae (B.Braun Melsungen AG) serve as media inlets and outlets. Both are glued to the bioreactor for mechanical stability and sealing properties.

In the last step, the bioreactor was clamped together by metal clamps from the office supply, as demonstrated in Figure 5B and as a CAD model in Figure 5A. The assembled bioreactor can be sterilized with 70% ethanol. Alternatively, the bioreactor is fully autoclavable, except for the polyethylene tubings and cannulae.

Cell Cultivation: Caco-2 cell line, collagen I, EGTA, and forskolin were purchased from Sigma Aldrich. Eagle's minimum essential medium (EMEM) was supplemented with 2 mmol L^{-1} glutamine, 1% non-essential amino acids, 1% penicillin/streptomycin, and 10% fetal bovine serum. The membrane used in the bioreactor for the cell support was a track-edged PET membrane (0.4 μm pore size, Sabeu GmbH). The membrane was coated with collagen I by filling the chambers with a 50 μg mL^{-1} collagen solution for 2 h at 37 °C. Afterward, the collagen solution was discarded, and the chamber was filled with 2×10^6 cells mL^{-1} Caco-2 cells.

Two hours after inoculation, the bioreactor was emptied and refilled with a fresh medium to remove the unattached cells from the bioreactor system. After 24 h of static cultivation, the bioreactor system was connected to a peristaltic pump and a medium reservoir containing 15 mL EMEM. Subsequently, medium circulation through the upper chamber was initiated, and the culture was kept under flow conditions for the rest of the experiment. If not stated otherwise, the pump was set to 150 μL min^{-1}, leading to a mean shear rate of 0.0036 dyne cm^{-2}. The bioreactor was kept in the incubator at 37 °C and 5% CO_2, and only transferred to the sterile workbench for medium exchange twice a week.

For the experiments with EGTA and forskolin, cell culture media containing either 10 mM EGTA or 10 μM forskolin were pumped into the reactor, and impedance spectra were recorded every minute to measure the immediate response of an at least 6-day-old cell layer. After 35 min, the EGTA-containing medium was removed and replaced by an EGTA-free medium.

Monitoring Cell-Layer Response with EIS: The EIS measurements were performed in galvanostatic mode with an amplitude of 10 μA and a frequency range from 10 Hz to 30 kHz. The impedance data were analyzed with the fitting software Zview 2 (Version 3.5b, Scribner Associates Inc., SP, USA). EIS monitored the response of Caco-2 cell-barrier to EGTA and forskolin. A complete spectrum was measured every 2 min. All impedance data were fitted with the equivalent circuit shown in Supporting Information. If the apical side differed only slightly from the basal side, the resistances and capacitances were combined according to $TEER = R_1 + R_2$ and $C^{-1} = C_1^{-1} + C_2^{-1}$, where TEER is the transepithelial electrical resistance and C, the total membrane capacitance. This allows comparison to data from other studies that modeled the cell layer with one resistor and capacitor in parallel. The quality of the fitting regarding the electrical equivalent circuit was evaluated by the chi-square method.

COMSOL Simulation: The simulation of the shear stress and sensitivity distributions on the membrane area was performed by COMSOL Multiphysics (vers. 5.3 COMSOL Inc., Burlington, MA) with the single-phase flow and AC/DC module. For electric field simulation, the relative permittivity of the medium was set to 78 and the electrical conductivity to 1.5 S m^{-1}. For shear stress simulation, the preset values for water were used (viscosity, 1.002 mPas; temperature 293.15 K; and density, 998 kg m^{-3}). Simulating the fluid-flow profile reveals the shear stress applied to the cells. Three different volume flows (0.05 mL min^{-1}, 0.5 mL min^{-1}, and 5 mL min^{-1}) were simulated. The shear stress data distributions on the cell culture area are reported as box plots in Figure 1.

Sensitivity Distribution: A uniform current density generated by the electrodes across the cellular monolayer is favorable; otherwise, the impedance may be systematically over- or underestimated.[37,45] Sensitivity defines the compartmental contribution of a region to the overall impedance.[46] Especially in four-electrode EIS, not every volume element contributes equally to the impedance measurement. The method of sensitivity distribution is described in detail by Grimnes and Martinsen.[36] In short, a current was injected between the two current-carrying electrodes, and the current density J_{CC} (A m^{-2}) was computed. The current density is a vector quantity with a magnitude and direction. In a second step, the same current was injected between the voltage pick-up electrodes, and computation of the current density J_{PU} (A m^{-2}) in each volume element was repeated. The vector dot product of the computed current densities J_{CC} and J_{PU}, divided by the current I (A) squared, equals the sensitivity distribution S [1/m^4] of each volume element.

$$S = \frac{J_{CC} \times J_{PU}}{I^2} \tag{1}$$

Most interesting hereby is the sensitivity distribution on the cultivation area and is shown in Figure 2B.

Supporting Information

Supporting Information is available from the Wiley Online Library or from the author.

Acknowledgements

This work received funding from the European Research Council (ERC) under the European Union's Horizon 2020 research and innovation program (grant agreement no. 694946). Part of the work was performed at the Center for Chemical Polymer Technology (CPT), which is supported by the EU and the federal state of North Rhine-Westphalia (grant no. EFRE 30 00 883 02).

Open access funding enabled and organized by Projekt DEAL.

Conflict of Interest

The authors declare no conflict of interest.

Data Availability Statement

The data that supports the findings of this study are available in the supplementary material of this article.

Keywords

Caco-2, 3D-printing, electrical impedance spectroscopy, organ-on-a chip, transepithelial electrical resistance

Received: January 4, 2021
Revised: February 22, 2021
Published online: May 6, 2021

[1] S. Tsukita, M. Furuse, M. Itoh, *Nat. Rev. Mol. Cell Biol.* **2001**, *2*, 285.
[2] R. Cecchelli, V. Berezowski, S. Lundquist, M. Culot, M. Renftel, M.-P. Dehouck, L. Fenart, *Nat. Rev. Drug Discovery* **2007**, *6*, 650.
[3] U. Mirastschijski, R. Dembinski, K. Maedler, *Front. Med.* **2020**, *7*, 254.
[4] K. Benson, S. Cramer, H.-J. Galla, *Fluids Barriers CNS* **2013**, *10*, 5.
[5] S. N. Bhatia, D. E. Ingber, *Nat. Biotechnol.* **2014**, *32*, 760.
[6] I. Bischoff, M. C. Hornburger, B. A. Mayer, A. Beyerle, J. Wegener, R. Fürst, *Sci. Rep.* **2016**, *6*, 1.
[7] J. R. Macdonald, W. B. Johnson, in *Impedance Spectroscopy: Theory, Experiment, and Applications*, Wiley, New York **2018**, pp. 1–20.
[8] H. J. Kim, D. Huh, G. Hamilton, D. E. Ingber, *Lab Chip* **2012**, *12*, 2165.
[9] A. Bein, W. Shin, S. Jalili-Firoozinezhad, M. H. Park, A. Sontheimer-Phelps, A. Tovaglieri, A. Chalkiadaki, H. J. Kim, D. E. Ingber, *Cell. Mol. Gastroenterol. Hepatol.* **2018**, *5*, 659.
[10] S. Giusti, T. Sbrana, M. La Marca, V. Di Patria, V. Martinucci, A. Tirella, C. Domenici, A. Ahluwalia, *Biotechnol. J.* **2014**, *9*, 1175.
[11] M. W. van der Helm, O. Y. Henry, A. Bein, T. Hamkins-Indik, M. J. Cronce, W. D. Leineweber, M. Odijk, A. D. van der Meer, J. C. Eijkel, D. E. Ingber, *Lab Chip* **2019**, *19*, 452.
[12] L. C. Delon, Z. Guo, A. Oszmiana, C.-C. Chien, R. Gibson, C. Prestidge, B. Thierry, *Biomaterials* **2019**, *225*, 119521.
[13] R. Lentle, P. Janssen, *J. Comp. Physiol. B* **2008**, *178*, 673.
[14] L. Cacopardo, J. Costa, S. Giusti, L. Buoncompagni, S. Meucci, A. Corti, G. Mattei, A. Ahluwalia, *Biosens. Bioelectron.* **2019**, *140*, 111340.
[15] D. Huh, Y.-s. Torisawa, G. A. Hamilton, H. J. Kim, D. E. Ingber, *Lab Chip* **2012**, *12*, 2156.
[16] L. J. Y. Ong, A. Islam, R. DasGupta, N. G. Iyer, H. L. Leo, Y.-C. Toh, *Biofabrication* **2017**, *9*, 045005.
[17] N. Bhattacharjee, A. Urrios, S. Kang, A. Folch, *Lab Chip* **2016**, *16*, 1720.
[18] J. Lölsberg, J. Linkhorst, A. Cinar, A. Jans, A. J. Kuehne, M. Wessling, *Lab Chip* **2018**, *18*, 1341.
[19] A. Jans, J. Lölsberg, A. Omidinia-Anarkoli, R. Viermann, M. Möller, L. De Laporte, M. Wessling, A. J. Kuehne, *Polymers* **2019**, *11*, 1887.
[20] C. M. Costello, M. B. Phillipsen, L. M. Hartmanis, M. A. Kwasnica, V. Chen, D. Hackam, M. W. Chang, W. E. Bentley, J. C. March, *Sci. Rep.* **2017**, *7*, 12515.
[21] J. L. Erkal, A. Selimovic, B. C. Gross, S. Y. Lockwood, E. L. Walton, S. McNamara, R. S. Martin, D. M. Spence, *Lab Chip* **2014**, *14*, 2023.
[22] J. Kieninger, A. Weltin, H. Flamm, G. A. Urban, *Lab Chip* **2018**, *18*, 1274.
[23] C. Probst, S. Schneider, P. Loskill, *Curr. Opin. Biomed. Eng.* **2018**, *6*, 33.
[24] O. Y. Henry, R. Villenave, M. J. Cronce, W. D. Leineweber, M. A. Benz, D. E. Ingber, *Lab Chip* **2017**, *17*, 2264.
[25] L. M. Griep, F. Wolbers, B. de Wagenaar, ter P. M. Braak, B. Weksler, I. A. Romero, P. Couraud, I. Vermes, A. D. van der Meer, A. van den Berg, *Biomed. Microdevices* **2013**, *15*, 145.
[26] H.-Y. Tan, S. Trier, U. L. Rahbek, M. Dufva, J. P. Kutter, T. L. Andresen, *PLoS One* **2018**, *13*, e0197101.
[27] T. Sbrana, N. Ucciferri, M. Favrè, S. Ahmed, E.-M. Collnot, C.-M. Lehr, A. Ahluwalia, M. Liley, *Sens. Actuators, B* **2016**, *223*, 440.
[28] R. Booth, H. Kim, *Lab Chip* **2012**, *12*, 1784.
[29] G. Linz, S. Djeljadini, L. Steinbeck, G. Köse, F. Kiessling, M. Wessling, *Biosens. Bioelectron.* **2020**, *165*, 112345.
[30] D. H. Elbrecht, C. J. Long, J. J. Hickman, *tc* **2016**, *1*, 1.
[31] B. Srinivasan, A. R. Kolli, M. B. Esch, H. E. Abaci, M. L. Shuler, J. J. Hickman, *J. Lab. Autom.* **2015**, *20*, 107.
[32] H. Schwan, *Biophysik* **1966**, *3*, 181.
[33] P. B. Ishai, M. S. Talary, A. Caduff, E. Levy, Y. Feldman, *Meas. Sci. Technol.* **2013**, *24*, 102001.
[34] H. P. Schwan, C. D. Ferris, *Rev. Sci. Instrum.* **1968**, *39*, 481.
[35] J. Winkler, P. Hendriksen, N. Bonanos, M. Mogensen, *J. Electrochem. Soc.* **1998**, *145*, 1184.
[36] S. Grimnes, Ø. G. Martinsen, *J. Phys. D: Appl. Phys.* **2006**, *40*, 9.
[37] J. Yeste, X. Illa, C. Gutiérrez, M. Solé, A. Guimerà, R. Villa, *J. Phys. D: Appl. Phys.* **2016**, *49*, 375401.
[38] A. H. Gitter, J.-D. Schulzke, D. Sorgenfrei, M. Fromm, *J. Biochem. Biophys. Methods* **1997**, *35*, 81.
[39] C.-M. Lo, C. R. Keese, I. Giaever, *Biophys. J.* **1995**, *69*, 2800.
[40] J. Wegener, D. Abrams, W. Willenbrink, H.-J. Galla, A. Janshoff, *Biotechniques* **2004**, *37*, 590.
[41] S. M. Krug, M. Fromm, D. Günzel, *Biophys. J.* **2009**, *97*, 2202.
[42] B. Tuo, G. Wen, Y. Zhang, X. Liu, X. Wang, X. Liu, H. Dong, *Am. J. Physiol.: Cell Physiol.* **2009**, *297*, C503.
[43] K.-M. Kreusel, M. Fromm, J. Schulzke, U. Hegel, *Am. J. Physiol.: Cell Physiol.* **1991**, *261*, C574.
[44] T. Tamada, M. J. Hug, R. A. Frizzell, R. J. Bridges, *JOP* **2001**, *2*, 219.
[45] B. Jovov, N. Wills, S. A. Lewis, *Am. J. Physiol.: Cell Physiol.* **1991**, *261*, C1196.
[46] O. I. Shuvo, M. N. Islam, *Dhaka Univ. J. Sci.* **2016**, *64*, 7.